A computational study to investigate the effect of defect geometries on the fatigue crack driving forces in powder-bed AM materials

Saikumar R. Yeratapally[1]
National Institute of Aerospace, Hampton, Virginia, 23666, USA

Christapher G. Lang[2], and Edward H. Glaessgen[3]
NASA Langley Research Center, Hampton, Virginia, 23681, USA

Powder-bed additive manufacturing (AM) processes are associated with the formation of multiple types of process-specific pores, including but not limited to lack-of-fusion (LoF) and keyhole pores. The performance of an AM component is dependent on the type of pores, their density and their proximity to the free surface, and other heterogeneities in the microstructure. In order to characterize the influence of porosity on the mechanical behavior of AM materials, it is imperative to quantitatively analyze the heterogeneous strain accumulation in the vicinity of porosity. Process-specific microstructure models are generated using SPPARKS, an open-source process simulation code. Spherical keyhole or irregular LoF pores are embedded into the microstructure models, which are meshed and input into a finite element code, ScIFEN, to solve for the heterogeneous strain localization in the vicinity of the pores. Given the non-smooth geometries of LoF pores, they readily promote strain accumulation in their vicinity thereby increasing the propensity of initiating fatigue cracks.

Nomenclature

C_{11}, C_{12}, C_{44} = cubic elastic constants
N_{SS} = number of slip systems
$\dot{\gamma}^{\alpha}$ = shear rate for slip system α
$\dot{\gamma}_o$ = reference shear rate
τ^{α} = resolved shear stress on slip system α
g^{α} = critical resolved shear stress on slip system α
g_o^{α} = initial resolved shear stress for slip system α
g_s^{α} = saturation resolved shear stress for slip system α
H_o, G_o = direct hardening coefficients
$\hat{n}_p$ = slip plane normal
μ = elastic constant
m = shear rate sensitivity parameter
β = calibration parameter
b = Burgers vector
ε_{zz} = strain component in the loading direction (ZZ)
x_o = x-coordinate of the centroid of microstructure volume
y_o = y-coordinate of the centroid of microstructure volume
z_o = z-coordinate of the centroid of microstructure volume
x = x-coordinate of any generic voxel inside a pore
y = y-coordinate of any generic voxel inside a pore

[1] Research Engineer, National Institute of Aerospace.
[2] Research Engineer, Structural Mechanics and Concepts Branch, NASA Langley Research Center.
[3] NASA Senior Technologist for Computational Materials, NASA Langley Research Center.

z = z-coordinate of any generic voxel inside a pore
A = scaling parameter of major axes of super ellipsoid
B = scaling parameter of semi-major axes of super ellipsoid
C = scaling parameter of minor axes of super ellipsoid
n = shape control parameter of super ellipsoid
e = shape control parameter of super ellipsoid

I. Introduction

Striving to meet the demands of product and systems design engineers, the materials design community is looking for ways to reduce the time taken in the materials design, development and certification stages, which is also a proposed goal of the materials genome initiative (MGI) [1]. The advent of additive manufacturing (AM) has created an opportunity for an integrated product and material design and has also paved a path forward for the 'design of materials for functionality' thereby creating a potential paradigm shift from the traditional empirical, iterative and often laborious materials development procedures [2]. Effectively using AM techniques would help achieve the goals of MGI.

AM processing techniques, such as the powder-bed fusion process, come with a large space of process parameters which means that it is far too expensive and time consuming to produce hundreds of components using various build parameters and characterizing scatter in properties. Such a large build and test matrix would not serve the purpose of MGI. An effective way to overcome this barrier is to seek a digital transformation in the way additively manufactured materials are designed, tailored and certified. An integrated computational materials engineering (ICME) framework that integrates AM process modeling simulations with performance predictive models would help narrow the process window, which in turn assists the processing/production engineer to significantly reduce the amount of time and effort spent in exploring the process parameter space.

In addition to having a large process parameter space, powder-based AM processes are associated with the formation of multiple types of process-specific defects (or pores), including but not limited to: i) horizontal lack-of-fusion (LoF) pores formed due to low power and high speed processing conditions [3-6], ii) vertical LoF pores formed as a result of a large hatch spacing [6], iii) keyhole pores formed due to high laser energy [4,5], iv) entrapped gas pores formed due to entrapped gas present in powder particles [5] and, v) oxide pores [7]. The performance of as-built components is directly dependent on the type of pores, their density and their local stress state, in addition to the complex crystallographic and morphological attributes of the microstructure of the material.

Over the past decade, significant research effort was dedicated towards studying the influence of process parameters on the: i) melt pool dimensions [8-12], ii) types and distribution of pores within the bulk of the material [4-7,13,14] and iii) tensile [15] and fatigue behavior [16-21] of as-built components due to the formation of pores. Computational models have been developed to quantitatively link the process parameters to size, shape, distribution and volume fraction of pores in as-built materials [22-26]. Tang et al. [22, 23], using a purely geometric framework, developed a 2D model to predict the volume fraction and shape of lack-of-fusion pores. Panwisawas et al. [24], using a computational fluid dynamics and heat transfer model, was able to predict the formation of keyhole pores. Prithivirajan et al. [27] studied the micromechanical response of idealized spherical pores in an SLM built IN718 alloy that underwent stress relief heat treatment followed by homogenization and aging processes. Using crystal plasticity finite element (CPFE) simulations, he predicted a critical pore size beyond which fatigue crack initiation occurs near the vicinity of pores rather than at crystallographic features. Cunningham et al. [28], using a CPFE framework, calculated strain localization around idealized pores in hot isostatically pressed (HIPed) material and as-built material, and showed that strain localizations in the as-built material to be significantly higher compared to those in HIPed material. Using an analytical model representing an isolated pore in a homogeneous elastic medium, Sabotka et al. [29] showed maintaining a spherical pore geometry and reducing the pore size are desirable to promote higher fatigue lives. This study suggests highly irregular pores have a much higher influence on fatigue performance than do nearly spherical keyhole and entrapped gas pores for SLM built material.

Although there have been several experimental and computational studies in the past decade that focused on characterizing defects [4-7,13,14, 22, 23] and understanding the effect of pores on the tensile [15] and fatigue [6,16-21] behavior of SLM-built materials, there have not been any extensive studies that focused on unifying high-fidelity process-simulation tools and property-predictive tools with a goal of understanding the effect of process-specific

defects on micro-scale fatigue crack driving forces. The current study aims to fill this gap by taking advantage of an integrated computational materials framework that solves for the micromechanical response within process-specific, defect-embedded microstructure instantiations. The micromechanical response and fatigue crack driving forces, expressed as the fatigue indicator parameter (or FIP), are evaluated in the vicinity of an idealized non-spherical lack-of-fusion pore with sharp features and an idealized spherical keyhole pore.

Inconel-718 (IN718), a nickel-based superalloy known for its high strength, excellent oxidation, wear, and corrosion resistance at high temperatures, is widely employed in high temperature components for engines and other high temperature structural applications. Additionally, its excellent weldability characteristic makes it a preferred material among superalloys to produce high-temperature components using the powder-bed selective laser melting (SLM) AM technique. There are several IN718 components for the RS-25 engine for the space launch system (SLS) identified to be manufactured by SLM [30, 31]. Owing to the aforementioned properties and applications, IN718 has been selected as a material of choice in the proposed study.

A detailed overview of the process-structure-property (PSP) framework is provided in Section II. Section III discusses the procedure in which LoF and keyhole pores are modelled into the microstructure domain. Section IV compares the micromechanical model response in the vicinity of idealized LoF and keyhole pores. Conclusions of the study are presented in Section V.

II. Process-structure-property framework

The computational materials-based PSP framework used in the current study is equipped with three important modules. The first module uses an open-source process-simulation tool, Stochastic Parallel PARticle Kinetics Simulator (SPPARKS) [32], from Sandia National Labs. It helps link process parameters of the SLM technique to the material microstructure by outputting a process-specific three dimensional microstructure instantiation. The second module uses open source packages, DREAM.3D [33] and Gmsh [34], to discretize the microstructure instantiation volume. The third module is an in-house property-predictive finite element driver, ScIFEN [35], that solves for the heterogeneous stress state within the process-specific microstructure output from SPPARKS. Both ScIFEN and SPPARKS are built to leverage high-performance computing architectures and are scalable over thousands of processors. A high level overview of the PSP framework is shown in Fig. 1.

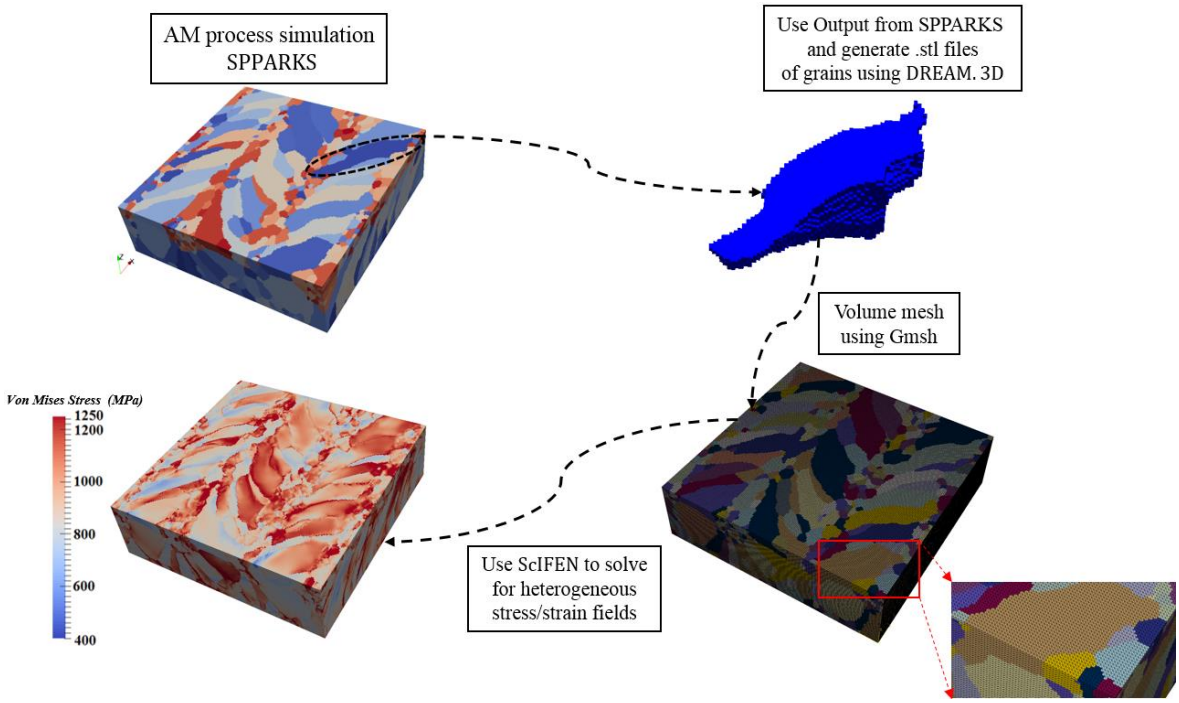

Fig. 1 A high level overview of the PSP framework leveraging SPPARKS, DREAM.3D, Gmsh and ScIFEN.

A. Process simulation and incorporation of texture

SPPARKS is a kinetic Monte Carlo (kMC) framework that implements an idealized molten zone and temperature-dependent grain boundary mobility to predict the three-dimensional microstructure in metallic materials produced through irregular grain growth [36]. It segregates the melt pool into two distinct non-overlapping regions, the fusion zone surrounded by the heat-affected zone. The temperature within the fusion zone is at or above the melting temperature and is simulated by assigning random spins to every lattice point within the region, thereby resulting in a high configurational energy [37]. The heat-affected zone on the other hand governs the grain boundary mobility defined by an Arrhenius relationship. Although the current version of SPPARKS [32] does not take in the laser specific process parameters directly, it accepts the parameters in the form of melt pool dimensions, separately for the fusion and the heat affected zones. The melt pool dimensions are solved from the process parameters using the analytical Rosenthal equation [38]. Using a finite element model to solve for the melt pool dimensions as a function of process parameters is beyond the scope of the current work and is a focus of future studies. The parameters that are input into SPPARKS include melt pool width, depth, tail length, cap height for both the fusion and heat affected zones, mobility parameter, hatch rotation, hatch spacing, and laser raster pattern. It must be noted that SPPARKS does not model the heat source directly, only the effect of the heat source is manifested through melt pool dimensions. Additionally, it lacks the complex physics that captures the mechanics of formation of keyhole pores. For a detailed explanation of the underlying kMC algorithm of SPPARKS, the reader is referred to the work of Rodgers et al. [36, 37].

The current version of SPPARKS [32] does not incorporate material texture [36]. Hence, texture definitions (or individual grain orientations) for microstructure instantiations output from SPPARKS simulations are sampled from observed textures obtained through electron back-scatter diffraction (EBSD) analysis of microstructures of IN718 samples built through the SLM process. The process parameters examined include a laser power of 200 W, velocity of 900 mm/sec, layer thickness of 30 μm, hatch spacing of 0.12 mm, and a hatch rotation of 0 degrees. A strong <100> texture observed from the EBSD analysis of one of the samples built using the aforementioned parameters is shown in Fig. 2.

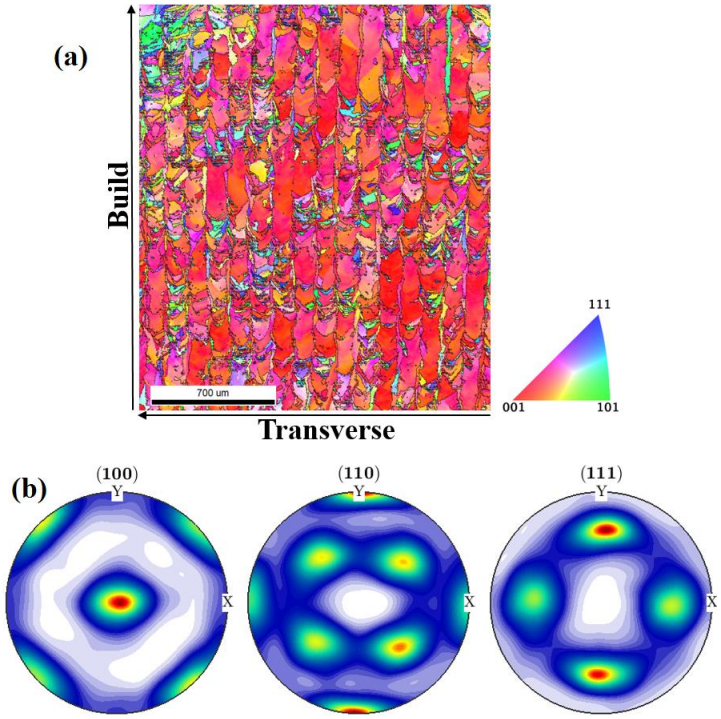

Fig. 2 (a) EBSD scan of an SLM built IN718 material, (b) Corresponding (100), (110) and (111) pole figures generated from the EBSD scan shown in Fig. 2a.

B. Volume meshing of microstructure instantiations

The microstructures from SPPARKS are fed into the DREAM.3D package for cleaning up the bad neighborhood data, which primarily consist of a few isolated voxels that are unmerged into the neighboring features. For instance, there could be a grain occupying just one voxel, which is most certainly an artifact from the kMC simulation. Using 'minimum feature size' and minimum neighbors as filters, the bad data is filtered and a refined microstructure is generated. The surface mesh of the microstructure is generated and STL files of each individual grain is exported into Gmsh, which is then able to produce the volume mesh of the entire microstructure volume. Quadratic tetrahedral elements are used to discretize the microstructure.

C. Crystal plasticity finite element framework

A CPFE framework was used to solve for the heterogeneous stress state within the polycrystalline microstructure by combining anisotropic elasticity with rate dependent crystal plasticity kinetics. For the elastic behavior, individual grains representing the γ –γ' matrix were assigned cubic elastic constants C_{11}, C_{12} and C_{44} equal to 259.6 GPa, 179.0 GPa, 109.6 GPa, respectively [39]. Since the experiments were conducted at room temperature, it has been assumed that the plastic flow occurs only through dislocation glide on cubic slip systems within the γ -γ' matrix, while octahedral slip is not activated. The flow rule used for describing incremental slip on the cubic slip systems is shown in Eq. 1

$$\dot{\gamma}^{\alpha} = \dot{\gamma}_{o} \frac{\tau^{\alpha}}{g^{\alpha}} \left| \frac{\tau^{\alpha}}{g^{\alpha}} \right|^{\frac{1}{m}-1} , \tag{1}$$

where $\dot{\gamma}^{\alpha}$ and $\dot{\gamma}_{o}$ are the shear and reference shear rates of slip system α, respectively, m is a shear rate sensitivity parameter, τ^{α} is the resolved shear stress acting on a slip system α, and g^{α} is the critical resolved shear stress representing the threshold for the onset of plastic deformation.

The slip resistance ($\dot{g}^{\alpha}$) shown in Eq. 2 evolves according to a gradient based evolution law obtained from combining the hardening laws given by Beaudoin et al. [40] and Voce-Kocks relations [41],

$$\dot{g}^{\alpha} = H_{o} \frac{\beta^{2}\mu^{2}b}{2(g^{\alpha} - g_{o}^{\alpha})} \sum_{k=1}^{N_{SS}} \sqrt{\left(\hat{n}_{p}^{k} : \Delta^{T}\right)\left(\Delta : \hat{n}_{p}^{k}\right)} \left|\dot{\gamma}^{k}\right| + G_{o} \left(\frac{g_{s}^{\alpha} - g^{\alpha}}{g_{s}^{\alpha} - g_{o}^{\alpha}}\right) \sum_{k=1}^{N_{SS}} \left|\dot{\gamma}^{k}\right| , \tag{2}$$

where g_{o}^{α} and g_{s}^{α} are the initial and saturation resolved shear strengths of slip system α, N_{SS} represents the number of slip systems, H_o and G_o are the direct hardening coefficients, $\beta = \frac{1}{3}$ [42], b is the Burgers vector, $\hat{n}_p$ is the slip plane normal, μ an elastic constant equal to C_{44}, Δ is the measure of dislocation density and is calculated using the gradient of plastic deformation as shown in Eq. 3,

$$\Delta_{ij} = \epsilon_{jkl} F^{p}_{il,k} . \tag{3}$$

There are a total of 6 calibration parameters ($\dot{\gamma}_o$, m, H_o, G_o, g_o^{α}, and g_s^{α}) in the crystal plasticity model used in the current framework. The parameters were tuned in order to fit the macroscopic stress strain curve of IN718 at room temperature. The final calibration parameters of the crystal plasticity framework are shown in Table 2.

Table 2. Calibrated parameters to fit the macroscopic stress strain curve of SLM built IN718 at room temperature.

Parameter	Value
$\dot{\gamma}_o$ (s^{-1})	0.98
m	0.045
H_o (MPa)	412.3
G_o (MPa)	415.2
g_o^{α} (MPa)	320.2
g_s^{α} (MPa)	375.2

The boundary conditions applied to the microstructure volume are depicted in the schematic shown in Fig. 3. The microstructure model is subjected to a 1% global strain by prescribing displacement-controlled loading conditions along with the other boundary conditions as depicted schematically in Fig. 3. 1% global strain was chosen to simulate a low-cycle fatigue loading condition where defects (like pores) dominate the microstructure in governing crack initiation. It must be noted that in this current study, the loading direction coincides with the build direction. Fully fixed constraints were applied on the bottom (-Z) face, whereas only the z-displacement was prescribed along the top (+Z) face. The remaining four faces (+X, -X, +Y and -Y) of the cuboidal microstructure domain were set to deform freely.

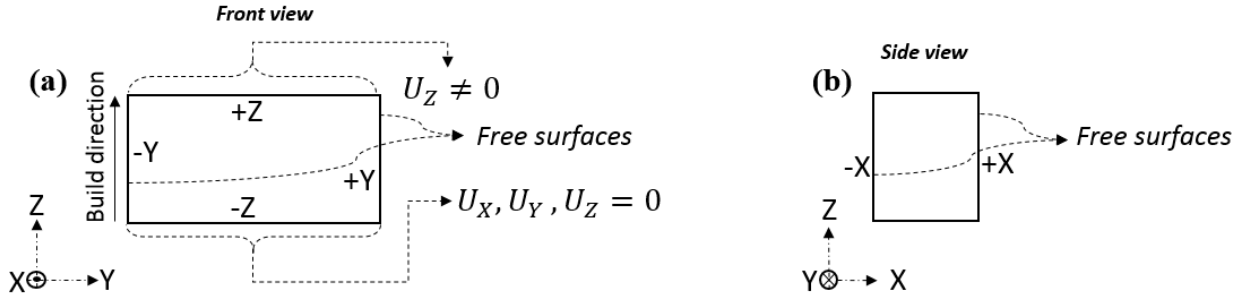

Fig. 3 (a) Front view of the microstructure domain showing the boundary conditions on +Z, +Y, -Z and -Y faces. (b) Side view of the microstructure domain showing the boundary conditions on the +X and -X faces.

III. Incorporation of pores into microstructure models

The PSP framework discussed in the current work does not take into consideration the formation of process-specific defects. Additionally, simulating the formation of process-specific defects is beyond the scope of the current work. Generation of process parameter-specific pores is the focus of a future effort. Hence, pores are embedded manually with the sole purpose of studying how differently shaped pores play a deleterious role in fatigue performance of the material.

The pore insertion algorithm used in the current study is detailed as follows:

i) A microstructure output from SPPARKS is refined using DREAM.3D to remove any existing bad features.

ii) Using analytical geometries (of a sphere/ellipsoid/super ellipsoid etc.,), define the region within the microstructure volume where a pore will be placed. In order to minimize the boundary effects, the pore is placed at the center of the microstructure volume. The voxels that lie within the volume, as defined by the analytical expression, are assigned a new and unique feature ID, thereby overwriting the previous IDs that define those voxels.

iii) Use DREAM.3D to create the surface meshes for all the features in the updated microstructure with the pore region defined.

iv) Delete the STL file of the pore region and input all the remaining STL files to Gmsh to create a volume mesh of the microstructure volume with the pore inserted.

The uniqueness of the aforementioned algorithm is that any number of pores of varying complex shapes can be embedded into the microstructure volume. Additionally, it provides the flexibility to define the density of pores and mean distance between the pores, thereby, creating an opportunity to evaluate the role played by various factors in degrading the fatigue performance. A drawback of the pore insertion methodology is that the pore volume needs to be defined by an analytical geometry, which is cumbersome to express for incorporation of more realistic pores. The pore volumes used in the current study are idealizations of the actual pores but replicate some important features that are evident from real pore geometries observed in SLM processes that were characterized through X-Ray micro CT scans [4,5]. A schematic of the pore insertion algorithm discussed above is shown in Fig. 4.

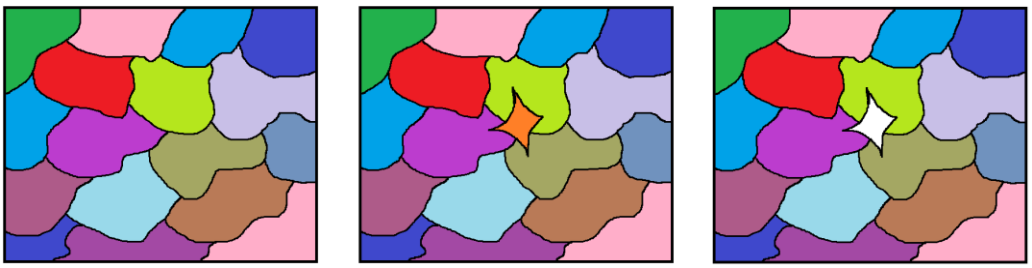

Fig. 4 (a) A schematic of a pristine microstructure, with grains and grain boundaries shown distinctly, (b) Microstructure with voxels of a desired arbitrary irregularly shaped region assigned a new grain (or feature) ID, (c) Microstructure showing the pore inserted at the desired region, by deleting the STL file of the region.

A. Incorporating idealized entrapped gas and keyhole pores

The morphology of entrapped gas pores is nearly spherical, but that of keyhole pores deviates from near-spherical geometry, although they are characterized by smooth morphologies, unlike LoF pores [5]. For the purpose of the current study, both entrapped gas and keyhole pores are idealized using a spherical morphology. An idealized spherical pore with radius R is introduced into the microstructure using the aforementioned algorithm. Assuming x_o, y_o and z_o represent the three coordinates of the centroid of the microstructure volume, the void region is determined by selecting all the voxels that satisfy Eq. 4, and identifying them as voxels that define the pore.

$$\frac{(x-x_o)^2+\left(y-y_o\right)^2+(z-z_o)^2}{R^2} \leq 1 \tag{4}$$

A spherical pore with R=6μm is inserted into the microstructure volume generated from SPPARKS. The CPFE framework is applied to analyze the strain localization in the vicinity of the pore, as shown in Fig. 5.

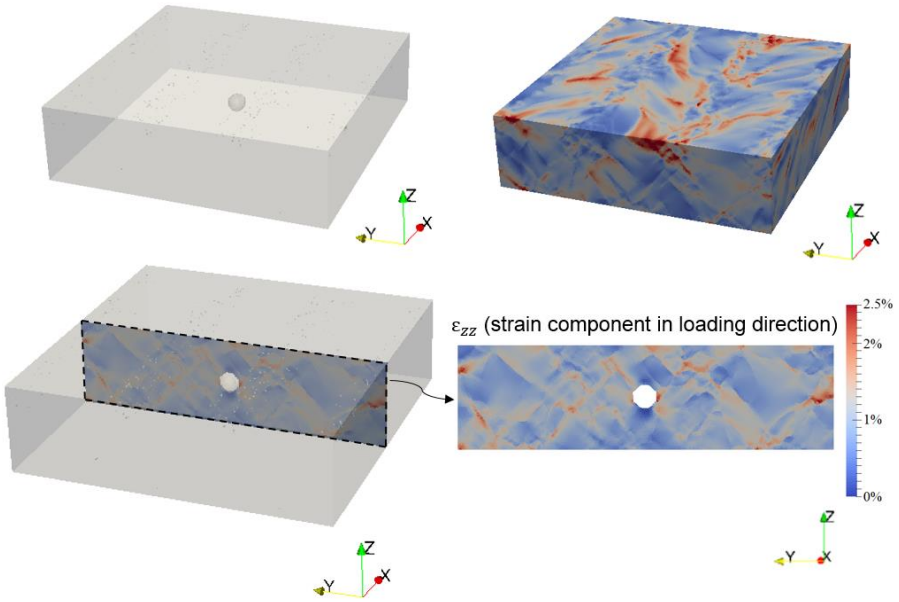

Fig. 5 A spherical pore representing an idealized entrapped gas or keyhole pore is embedded into the microstructure volume output from SPPARKS and analyzed using CPFE framework. Cut section view of the microstructure is shown to visualize the strain localization in the vicinity of the pore. Strain component in the loading direction (ZZ) is shown.

B. Incorporating idealized lack-of-fusion pores

LoF pores have highly irregular geometry characterized by high aspect ratios and sharp corners that act as drivers for strain localizations to occur that lead to initiation of fatigue cracks [5, 6, 43]. Large LoF pores generate high stress intensity factors and degrade the ductility of SLM built components, whereas small LoF pores are detrimental for promoting fatigue crack initiation [43]. These pores can potentially degrade the fatigue life of SLM built components by an order of magnitude compared to conventional wrought parts [44]. Hence, completely eliminating LoF pores is within the best interest of processing engineers, in order to improve the fatigue performance of the components.

For the purpose of capturing the sharp features and non-spherical geometries that are the major characteristics of LoF pores, they are modeled using analytical equations that define super ellipsoids. Using super ellipsoid geometries ensures that the pores are symmetrical, which is certainly not the case in reality, but for the purpose of the current study, the pore shapes are idealized. Assuming the LoF pore is defined by a super ellipsoid with A, B and C as scaling parameters along the three axes (these parameters are analogous to the lengths of major, semi-major and minor axes of an ellipsoid), and shape control parameters, e and n, the volume occupied by the LoF pore is defined using the equation of a super ellipsoid shown in Eq. 5. Figure 6 shows the dependence of the shape of the super ellipsoid on the parameters e and n.

$$\left(\left| \frac{x - x_o}{A} \right|^{\frac{2}{e}} + \left| \frac{y - y_o}{B} \right|^{\frac{2}{e}} \right)^{\frac{e}{n}} + \left| \frac{z - z_o}{C} \right|^{\frac{2}{n}} \leq 1 \tag{5}$$

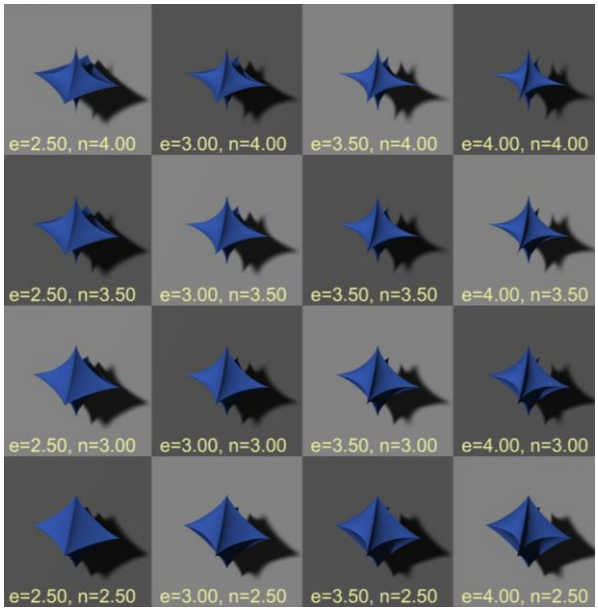

Fig. 6 Shape change in super ellipsoid geometry attributed to the parameters e and n. This image has been borrowed from a Wikipedia article on Super ellipsoids [45].

Assuming the values of scaling parameters, A, B and C, to be all equal to 12μm and the shape parameters e and n to be 4 and 2.5, respectively, a super ellipsoid pore is inserted into the microstructure instantiation output from SPPARKS, using the analytical expression shown in Eq. 5 and the algorithm discussed above. The CPFE framework is applied to analyze the strain localization in the vicinity of the pore, as shown in Fig. 7. The clip view shown in the figure clearly shows the high amount of strain localization near the sharp corner of the pore. This is the characteristic micro-mechanical behavior of the LoF pore which promotes crack initiation and growth and thereby degrades the performance of the component.

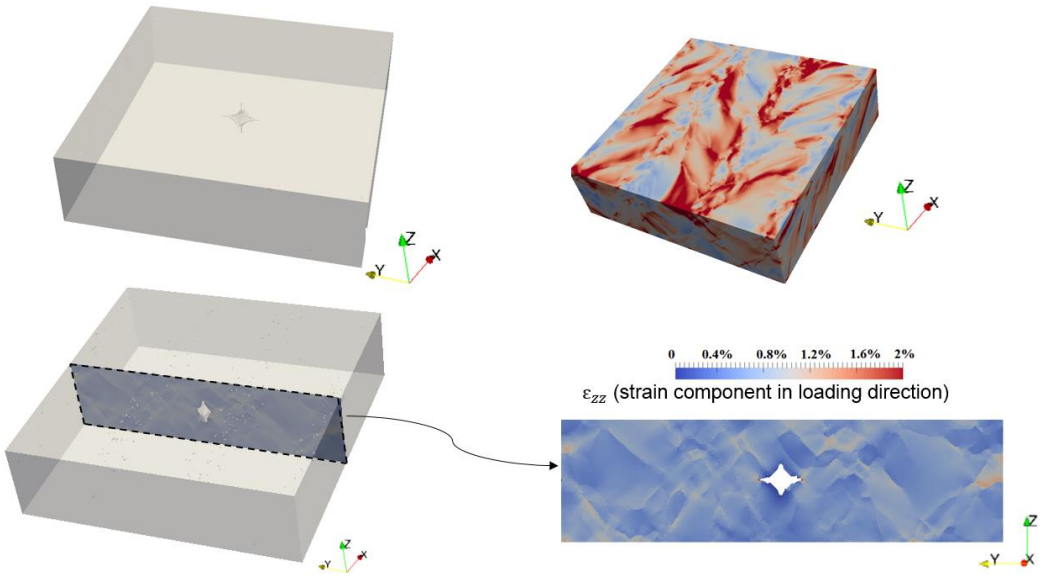

Fig. 7 A super ellipsoid representing an idealized LoF pore is embedded into the microstructure volume output from SPPARKS and analyzed using the CPFE framework. Cut section view of the microstructure is shown to visualize the strain localization in the vicinity of the pore. Strain component in the loading direction (ZZ) is shown.

IV. Comparing the effects of pores with different geometries

A case study has been undertaken to understand the effect of pore shapes on fatigue crack driving forces. As strain localization is a pre-cursor to fatigue crack initiation, the localization was measured through the accumulation of the strain component in the loading direction (ZZ). Two simulations were run, with one simulation having an idealized entrapped gas/keyhole pore and the other one having an idealized LoF pore. Pores were inserted into the same microstructure volume in order minimize the role played by the surrounding microstructure in controlling the strain localization. Additionally, the volume fraction of the pores in both the simulations were kept constant to eliminate the size effect and only focus on the pore geometry. A displacement controlled global strain of 1% was applied in both the simulations. A cut section view of the 3D strain localization maps of both the simulations is shown in Fig. 8.

In the case of the idealized entrapped gas/keyhole pore, shown in Fig. 8a, the strain localization in the vicinity of the pore is of similar magnitude when compared to the localizations in the rest of the microstructure far from the pore, where the influence of the pore is minimal. In this case, perhaps the fatigue crack initiation mechanism might be governed by the crystallographic features and less due to the presence of the pore. Using CPFE simulations, Veerappan et al. [27] showed that in order for the crack initiation to be governed by localizations in the vicinity of the pore rather than the crystallographic attributes, the spherical pore needs to attain a critical size. Based on the strain localization profile, it is evident that the size of the pore considered in the current study is smaller than the critical pore size which would promote higher strain accumulation near its vicinity.

For the simulation with an embedded idealized LoF pore, as shown in Fig. 8b, it can be visualized that the strain accumulation near the sharp corners is significantly higher than that of the localizations that occur in the rest of the microstructure, and certainly higher than the localizations near the vicinity of the spherical pore shown in Fig. 8a. The maximum value of ε_{ZZ} in the vicinity of the keyhole pore and the LoF pore shown in the cross-sections in Fig. 8a and 8b is 2.05% and 3.3%, respectively. In other words, for the particular size of keyhole and LoF pores studied in the current work, the LoF pore accumulates approximately 37.8% more strain in the loading direction. Over multiple fatigue cycles, high strain accumulation in the vicinity of LoF pores will increase the likelihood of the initiation of fatigue cracks.

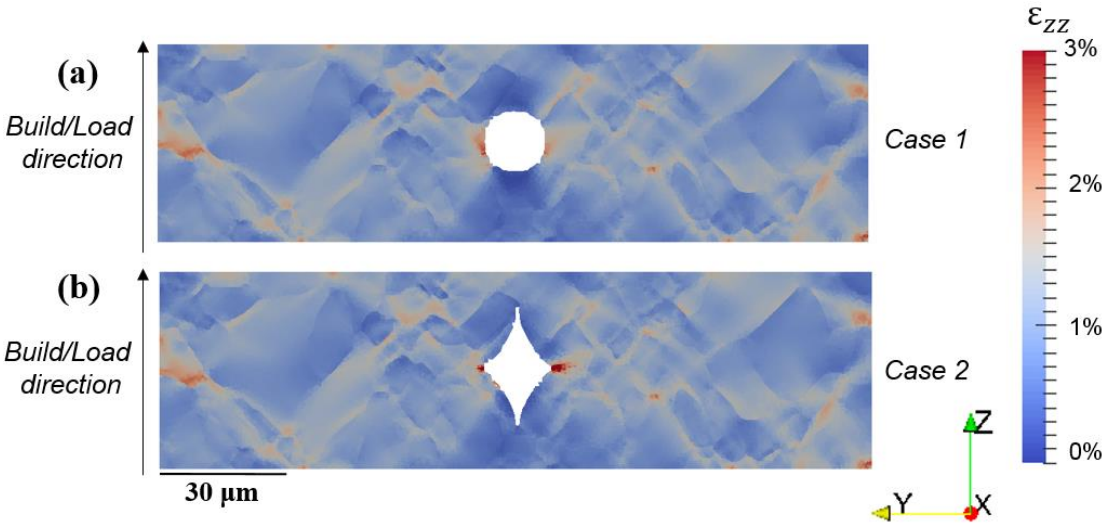

Fig. 8 Comparison of the strain accumulation in the vicinity of: a) an idealized gas/keyhole pore, and b) an idealized LoF pore. In both simulations, the microstructure surrounding the pore, volume fraction of the pore and the applied load are the same.

V. Conclusion

A process-structure-property (PSP) framework that leverages the capabilities of SPPARKS, a process simulation package, and ScIFEN, a scalable finite element driver is used to understand the effect of pore geometry on the fatigue performance of additively built IN718 material. A pore insertion algorithm, which aids in inserting idealized pores defined by analytical geometries, is discussed. Idealized entrapped gas/keyhole pores are modeled using a spherical geometry and lack of fusion (LoF) pores are modeled using super ellipsoid geometries to mimic the sharp features that are evident in LoF pores. Two simulations were run, with one simulation having an idealized entrapped gas/keyhole pore and the other having an idealized LoF pore. Pores were inserted into the same microstructure instantiation in order to minimize the role played by the surrounding microstructure in controlling the strain localization in the vicinity of the pore. The volume fraction of the pores in both simulations was maintained the same, in order to minimize the size-effect of the pore. It was observed that the strain localization in the vicinity of the LoF pore was about 37.8% higher than in the vicinity of keyhole pore of the same size as the LoF pore. The deleterious role played by the LoF pore in degrading the fatigue performance is evident from the high strain localization promoted by the sharp features of the pore. This informs the materials design and processing engineer regarding the importance of optimizing the process parameters so as to eliminate the formation of LoF pores. This can primarily be achieved by modulating the laser power, laser scan speed, and hatch spacing.

Acknowledgments

The authors would like to acknowledge funding for this project from the independent research and development program at NASA Langley Research Center and NASA Aeronautics Research Mission Directorate's Transformative Tools and Technologies project. The authors would like to thank Wesley A. Tayon for providing the EBSD scans of SLM built IN718 material, and Dr. Albert Cerrone for insightful discussions on the topic of process-induced porosity.

References

[1] Drosback, M., "Materials Genome Initiative: Advances and Initiatives," *Journal of Materials*, Vol. 66, No. 3, 2014, pp. 334-335.
[2] Kalidindi, S., "Materials Data Sciences and Informatics", *Coursera [Online course], URL:* https://www.coursera.org/learn/material-informatics [retrieved 14 May 2019].
[3] Tang, M., Pistorius, P. C., "Anisotropic Mechanical Behavior of AlSi10Mg Parts Produced by Selective Laser Melting," *Journal of Materials*, Vol. 69, No. 3, 2017, pp. 516-522.

[4] Cunningham, R., Narra, S. P., Montgomery, C., Beuth, J., Rollett, A.D., "Synchrotron-Based X-ray Microtomography Characterization of the Effect of Processing Variables on Porosity Formation in Laser Power-Bed Additive Manufacturing of Ti-6Al-4V," *Journal of Materials,* Vol. 69, No. 3, 2017, pp. 479-484.
[5] Cunningham, R., Narra, S. P., Ozturk, T., Beuth, J., Rollett, A.D., "Evaluating the Effect of Processing Parameters on Porosity in Electron Beam Melted Ti-6Al-4V via Synchrotron X-ray Microtomography," *Journal of Materials,* Vol. 68, No. 3, 2016, pp-765-771.
[6] Brown, A., Zachary, J., Tilson, W., "Classification, Effects, and Prevention of Build Defects in Powder-bed Fusion Printed Inconel 718," *NASA Report Number M17-5848,* 2017.
[7] Tang, M., Pistorius, P. C., "Oxides, Porosity and Fatigue Performance of AlSi10Mg Parts Produced by Selective Laser Melting," *International Journal of Fatigue,* Vol. 94, No. 2, 2017, pp. 192-201.
[8] Gong, H., Gu, H., Zeng, K., Dilip, J.J.S., Pal, D., Stucker, B., Christiansen, D., Beuth, J., Lewandowski, J.J., "Melt Pool Characterization for Selective Laser Melting of Ti-6Al-4V Pre-alloyed Powder," *Proceedings of the Solid Freeform Fabrication Symposium,* Austin, TX, USA, 2014, pp. 256–267.
[9] Dilip, J.J.S., Zhang, S., Teng, C., Zeng, K., Robinson, C., Pal, D., Stucker, B., "Influence of Processing Parameters on the Evolution of Melt Pool, Porosity, and Microstructures in Ti-6Al-4V Alloy Parts Fabricated by Selective Laser Melting," *Progress in Additive Manufacturing,* Vol. 2, No. 3, 2017, pp. 157-167.
[10] Cherry, J.A., Davies, H.M., Mehmood, S., Lavery, N.P., Brown, S.G.R., Sienz, J., "Investigation into the Effect of Process Parameters on Microstructural and Physical Properties of 316L Stainless Steel Parts by Selective Laser Melting," *International Journal of Advanced Manufacturing Technology,* Vol. 76, 2015, pp. 869-879.
[11] Gunenthiram, V., Peyre, P., Schneider, M., Dal, M., Coste, F., Fabbro, R., "Analysis of Laser–Melt Pool–Powder bed Interaction During the Selective Laser Melting of a Stainless Steel," *Journal of Laser Applications,* Vol. 29:022303, 2017.
[12] Kusuma, C., "The Effect of Laser Power and Scan Speed on Melt Pool Characteristics of Pure Titanium and Ti-6Al-4V alloy for Selective Laser Melting," Master's Thesis, Wright State Univ., Dayton, OH, 2016.
[13] Gong, H., Rafi, K., Gu, H., Starr, T., Stucker, B., "Analysis of Defect Generation in Ti–6Al–4V Parts made Using Powder Bed Fusion Additive Manufacturing Processes," *Additive Manufacturing,* Vol. 1, 2014, pp.87–98.
[14] Qiu, C., Kindi, M.A., Aladawi, A.S., Hatmi, I.A., "A Comprehensive Study on Microstructure and Tensile Behaviour of a Selectively Laser Melted Stainless Steel," *Scientific Reports,* Vol. 8:7785, 2017, pp. 1-16.
[15] Tang, M., Pistorius, P.C., "Anisotropic Mechanical Behavior of AlSi10Mg Parts Produced by Selective Laser Melting," *Journal of Materials,* Vol. 69, No. 3, 2017, pp. 516-522.
[16] Romano, S., Brückner-Foit, A., Brandão, A., Gumpinger, J., Ghidini, T., Beretta, S., "Fatigue Properties of AlSi10Mg Obtained by Additive Manufacturing: Defect-based Modelling and Prediction of Fatigue Strength," *Engineering Fracture Mechanics,* Vol. 187, 2018, pp. 165-189.
[17] Romano, S., Patriarca, L., Foletti, S., Beretta, S., "LCF Behaviour and a Comprehensive Life Prediction Model for AlSi10Mg Obtained by SLM," *International Journal of fatigue,* Vol. 117, 2018, pp. 47-62.
[18] Romano, S., Beretta, S., Brandão, A., Gumpinger, J., Ghidini, T., "HCF Resistance of AlSi10Mg Produced by SLM in Relation to the Presence of Defects," *Procedia Structural Integrity,* Vol. 7, 2017, pp. 101-108.
[19] Williams, S.T., Withers, P.J., Prangnell, P.B., "The Influence of Porosity on Fatigue Crack Initiation in Additively Manufactured Titanium Components," *Scientific Reports,* Vol. 7:7308, 2017, pp.1-13.
[20] Almatani, R.A., "The Effect of Pore Density and Distribution on Fatigue Weak Links in an A713 Cast Aluminum Alloy," Master's Thesis, College of Engineering, Univ. of Kentucky, Lexington, KY, 2017.
[21] Tang, M., Pistorius, P.C., "Fatigue Life Prediction for AlSi10Mg Components Produced by Selective Laser Melting," *International Journal of Fatigue,* Vol. 125, 2019, pp. 479-490.
[22] Tang, M., Pistorius, P.C., Beuth, J.L., "Prediction of Lack-of-Fusion Porosity for Powder Bed Fusion," *Additive Manufacturing,* Vol. 14, 2017, pp. 39-48.
[23] Tang, M., Pistorius, P.C., Beuth, J., "Geometric Model to Predict Porosity of Part Produced in Powder Bed System," *Proceedings of the Materials Science and Technology (MS&T) Conference,* Columbus, Ohio, 2015, pp. 129-135.
[24] Panwisawas, C., Perumal, B., Ward, R.M., Turner, N., Turner, R.P., Brooks, J.W., Basoalto, H.C., "Keyhole Formation and Thermal Fluid Flow-induced Porosity During Laser Fusion Welding in Titanium Alloys: Experimental and Modelling," *Acta Materialia,* Vol. 126, No. 1, 2017, pp.251-263.
[25] Khairallah, S.A., Anderson, A.T., Rubenchik, A., King, W.E., "Laser Powder-Bed Fusion Additive Manufacturing: Physics of Complex Melt Flow and Formation Mechanisms of Pores, Spatter, and Denudation Zones," *Acta Materialia,* Vol. 108, No. 1, 2016, pp. 36-45.
[26] Martin, A.A., Calta, N.P., Khairallah, S.A., Wang, J., Depond, P.J., Fong, A.Y., Thampy, V., Guss, G.M., Kiss, A.M., Stone, K.H., Tassone, C.J., Weker, J.N., Toney, M.F., van Buuren, T., Matthews, M.J., "Dynamics of Pore

Formation During Laser Powder Bed Fusion Additive Manufacturing," *Nature Communications*, Vol. 10, 2019, pp.1-10.
[27] Prithivirajan, V., Sangid, M.D., "The Role of Defects and Critical Pore Size Analysis in the Fatigue Response of Additively Manufactured IN718 via Crystal Plasticity," *Materials & Design*, Vol. 150, No. 1, 2018, pp. 139-153.
[28] Cunningham, R., Nicolas, A., Madsen, J., Fodran, E., Anagnostou, E., Sangid, M.D., Rollett, A.D., "Analyzing the Effects of Powder and Post-processing on Porosity and Properties of Electron Beam Melted Ti-6Al-4V," *Materials Research Letters*, Vol. 5, No. 7, 2017, pp. 516-525.
[29] Sobotka, J.C., Enright, M.P., McClung, R.C., "Application of Critical Distances to Fatigue at Pores," *Fatigue & Fracture of Engineering Materials & Structures*, 2019. doi:10.1111/ffe.13004.
[30] Clinton, R.G.,Jr., "Overview of Additive Manufacturing Initiatives at NASA Marshall Space Flight Center," *NASA Report Number MSFC-E-DAA-TN52216*, 2018.
[31] Grad, P.R., "Rapid Fabrication Techniques for Liquid Rocket Channel Wall Nozzels," *52nd AIAA/SAE/ASEE Joint Propulsion Conference*, July 25-27, 2016, Salt Lake City, UT
[32] SPPARKS Kinetic Monte Carlo Simulator, URL: https://spparks.sandia.gov/ [retrieved 20th May 2019].
[33] Groeber, M., Jackson, M., "DREAM.3D: a Digital Representation Environment for the Analysis of Microstructure in 3D," *Integrating Materials and Manufacturing Innovation*, Vol. 3, 2014, pp. 1-17.
[34] Geuzaine, C., Remacle, J.F., "Gmsh: a 3-D Finite Element Mesh Generator with Built-in Pre-and Post-Processing Facilities," *International Journal for Numerical Methods in Engineering*, Vol. 79, 2009, pp. 1309–1331. doi:10.1002/nme.2579.
[35] Warner, J.E., Bomarito, G.F., Hochhalter, J.D., "Scalable Implementation of Finite Elements by NASA _ Implicit (ScIFEi)," NASA/TM—2016–219180, 2016.
[36] Rodgers, T.M., Madison, J.D., Tikare, V., "Simulation of Metal Additive Manufacturing Microstructures using kinetic Monte Carlo," *Computational Materials Science*, Vol. 135, 2017, pp. 78–89.
[37] Rodgers, T.M., Madison, J.D., Tikare, V., Maguire, M.C., "Predicting Mesoscale Microstructural Evolution in Electron Beam Welding," *Journal of Materials*, Vol. 68, No. 5, 2016, pp. 1419 -1426.
[38] Rosenthal, D., "Mathematical Theory of Heat Distribution during Welding and Cutting," *Welding Journal*, Vol. 20, 1941, pp. 220–234.
[39] Haldipur, P., Margetan, F.J., Thompson, R.B., "Estimation of Single Crystal Elastic Constants from Ultrasonic Measurements on Polycrystalline Specimens," *AIP Conf Proc AIP*. Vol. 700, No. 1, 2004, pp.1061–1068.
[40] Beaudoin A.J., Acharya A., Chen S.R., Korzekwa, D.A., Stout, M.G., "Consideration of Grain-size Effect and Kinetics in the Plastic Deformation of Metal Polycrystals," *Acta Mater*, Vol. 48, 2000, pp. 3409–3423.
[41] Kocks, F., "Laws for Work-Hardening and Low-Temperature creep," *J Eng Mater Technol*, Vol. 98, pp. 76–85.
[42] Cerrone, A., Stein, C., Pokharel, R., Hefferan, C., Lind, J., Tucker, H., Suter R., Rollett, A., Ingraffea, A., "Implementation and Verification of a Microstructure-based Capability for Modeling Microcrack Nucleation in LSHR at Room Temperature," *Model Simul Mater Sci Eng*, Vol. 23:35006, 2015.
[43] Zhang, B., Ham, K., Shao, S., Shamsaei, N., Thompson, S.M., "Effect of Heat Treatment and Hot Isostatic Pressing on the Morphology and Size of Pores in Additive Manufactured Ti-6Al-4V Parts," *Proceedings of the 28th Annual International Solid Freeform Fabrication Symposium*, 2017, pp. 107-114.
[44] Yadollahi, A., Shamsaei, N., "Additive Manufacturing of Fatigue Resistant Materials: Challenges and Opportunities," *International Journal of Fatigue*, Vol. 98, 2017, pp. 14-31.
[45] "Superellipsoid," *Wikipedia*, URL: https://en.wikipedia.org/wiki/Superellipsoid/ [retrieved 22nd May 2019].